**Atmospheric
Chemistry
and Physics
Discussions**

Secondary aerosol formation from photochemical aging of aircraft exhaust in a smog chamber

M. A. Miracolo[1], C. J. Hennigan[1], M. Ranjan[1], N. T. Nguyen[1], T. D. Gordon[1], E. M. Lipsky[2], A. A. Presto[1], N. M Donahue[1], and A. L. Robinson[1]

[1]Center for Atmospheric Particle Studies, Carnegie Mellon University, Pittsburgh, PA, 15213, USA
[2]Penn State Greater Allegheny, McKeesport, PA, 15123, USA

Correspondence to: A. Robinson (alr@andrew.cmu.edu)

ACPD

10, 27893–27924, 2010

Secondary aerosol formation from aging of aircraft exhaust

M. A. Miracolo et al.

Title Page

Abstract	Introduction
Conclusions	References
Tables	Figures

| ◄◄ | ►► |
| ◄ | ► |

Back | Close

Full Screen / Esc

Printer-friendly Version

Interactive Discussion

Full Screen / Esc

Printer-friendly Version

Interactive Discussion

Abstract

Field experiments were performed to investigate the effects of photo-oxidation on fine particle emissions from an in-use CFM56-2B gas turbine engine mounted on a KC-135 Stratotanker airframe. Emissions were sampled into a portable smog chamber from a rake inlet installed one-meter downstream of the engine exit plane of a parked and chocked aircraft. The chamber was then exposed to sunlight and/or UV lights to initiate photo-oxidation. Separate tests were performed at different engine loads (4, 7, 30, 85%). Photo-oxidation created substantial secondary particulate matter (PM), greatly exceeding the direct PM emissions at each engine load after an hour or less of aging at typical summertime conditions. After several hours of photo-oxidation, the ratio of secondary-to-primary PM mass was on average 35 ± 4.1, 17 ± 2.5, 60 ± 2.2, and 2.7 ± 1.1 times the primary PM for the 4, 7, 30, and 85% load experiments, respectively. The composition of secondary PM formed strongly depended on load. At 4% load, secondary PM was dominated by secondary organic aerosol (SOA). At higher loads, the secondary PM was mainly secondary sulfate. Predictions of an SOA model are compared to the measured SOA formation. The SOA model predicts ~40% of the SOA produced during the 4% load experiment and ~60% for the 85% load experiment. Significant emissions of low-volatility compounds present in both the vapor- and particle-phase were measured in the exhaust and represent a significant pool of SOA precursors that appear to form SOA efficiently when oxidized. These results underscore the importance of accounting for atmospheric processing when assessing the influence of aircraft emissions on ambient PM levels.

1   Introduction

Airports are often located in areas with elevated air pollution levels and recent studies report that aircraft operations can contribute significantly to local and regional pollution (Carslaw et al., 2006; Unal et al., 2005; Dodson et al., 2009; Yu et al., 2004; Hu et al., 2009). In order to quantify the impacts of airports on ground-level air quality,

there is a need for improved understanding of both aircraft emissions and how those emissions evolve in the atmosphere. In this paper, we focus on the contribution of aircraft emissions to ambient fine particle mass (PM).

Aircraft exhaust contributes to ambient PM levels in two ways – primary aerosol emitted directly from aircraft and secondary aerosol formed as a result of photo-oxidation of exhaust in the atmosphere. Numerous studies have investigated primary aerosol emissions from aircraft (Agrawal et al., 2008; Petzold and Schvöder, 1998; Onasch et al., 2009; Wey et al., 2006; Kinsey et al., 2010; Wayson et al., 2009; Anderson, 2005). The magnitude and composition of these emissions strongly depend on engine load. Furthermore, as the exhaust is diluted and cooled downstream of an engine, the particle size and composition can evolve significantly (Onasch et al., 2009). The experiments performed in this study extend this work to include chamber experiments to isolate the effects of photo-oxidation on aircraft exhaust over longer atmospherically relevant timescales.

Recent experimental data has demonstrated that oxidative aging of exhaust from other combustion systems, including dilute diesel exhaust (Chirico et al., 2010) and woodsmoke (Grieshop et al., 2009c), results in substantial formation of secondary organic aerosol (SOA). It is likely that the same is true of aircraft exhaust. Aircraft emit significant quantities of volatile organic compounds, including known SOA precursors such as benzene and toluene (Anderson et al., 2006; Slemr et al., 1998; Agrawal et al., 2008; Spicer et al., 1999; Herndon et al., 2006; Herndon et al., 2009). The magnitude and composition of these gaseous emissions depend strongly on load, with much higher emissions at low engine loads. Wood et al. also found enhanced levels of HO_x in exhaust from idling engines (Wood et al., 2008). Therefore, the potential for ozone and secondary aerosol production should be significant. However, few studies have investigated the effects of photochemistry on aircraft emissions. Spicer et al. performed ozone reactivity experiments with emissions at idle power, concluding that the idle emissions were very reactive for ozone formation (Spicer et al., 1999). However, that study did not investigate the potential for secondary aerosol formation.

In this paper, we present results from smog chamber experiments of secondary aerosol formation from the photo-oxidation of aircraft exhaust. We describe the magnitude and composition of secondary aerosol formed at different engine loads. The data are then used to evaluate the performance of a SOA model. The paper concludes with a discussion of the relative importance of primary aerosol emissions versus secondary production. Better understanding of the evolution of PM emissions should improve models that predict the impact of these emissions throughout the atmosphere. Details on the composition and partitioning behavior of primary emissions are presented in a companion paper (Presto et al., 2010).

2 Experimental methods

2.1 Experimental setup

Emissions and photo-oxidation experiments were conducted in collaboration with the Pennsylvania Air National Guard 171st Air Refueling Wing at the Pittsburgh International Airport during a two-week period in July 2009. Seven separate experiments were performed to characterize emissions from a CFM56-2B gas turbine engine mounted on a KC-135 Stratotanker airframe. The CFM56 is one of the most widely used family of engines in the world, powering more than 8000 commercial and military aircraft (www.cfm56.com). Experiments were performed at different loads while the aircraft was parked and chocked. A summary of the experiments is listed in Table A1 in the Supplement. Test points were set based on fan speed (N1) to correspond to different engine thrusts including climb out (85% of maximum thrust), approach (30% of maximum thrust), idle (7% of maximum thrust), and minimum engine load (4% of maximum thrust). The engine was operated on standard JP-8 fuel; composition data for the fuel is listed in Table A2 in the Supplement.

A schematic of the experimental setup is shown in Fig. 1. Details of the sampling configuration are described in detail elsewhere (Presto et al., 2010). Briefly, emissions

were sampled through a rake inlet installed one-meter downstream of the engine exit plane. The rake consisted of three equally spaced inlets, with one centered on the oil vent and the other two installed 7.6 cm above and below the center inlet. The emissions were transferred into the chamber through a 21 m heated stainless steel transfer line held at 150 °C. The exhaust was pushed into the portable chamber using two parallel ejector dilutors (Dekati, model DI-100), which were operated with clean (HEPA and activated carbon filtered) and dry air. All surfaces in contact with the exhaust upstream of the smog chamber were maintained at 150 °C.

The smog chamber was a 7 m^3 Teflon bag suspended on an open metal frame. Before each experiment, the chamber was cleaned by flushing with HEPA and activated carbon filtered air. Prior to adding exhaust, the chamber was one-half to three-quarters filled with clean air at ambient temperature. The engine was run for several minutes at low load (4%), allowing time for warm-up, before the engine test point was set. Upon entering the chamber, the exhaust was further diluted, reducing its temperature to near ambient conditions. Exhaust was added to the chamber for fifteen to thirty minutes while the engine operated at steady-state conditions; initial particles concentrations inside the chamber ranged between 1 and 10 µg m^{-3}. The dilution ratio between the engine exit plane and chamber ranged between 30–125 across the set of experiments. During filing, the chamber was covered to prevent exposure to sunlight. Prior to photo-oxidation, the average initial chamber temperature was 23 ± 2.5 °C with a relative humidity of 14.7 ± 3.8% across the set of experiments. Since the portable smog chamber was located outside, it was subject to ambient temperature changes. The temperature in the chamber increased an average of 4.4 °C during photo-oxidation.

After allowing time for mixing, we characterized the primary emissions in the dark chamber for approximately one hour before exposing the chamber to light (initiating photo-oxidation). Photo-oxidation was initiated either by turning on banks of UV lights (Model F40BL UVA, General Electric) and/or removing the cover to expose the chamber to sunlight.

Secondary aerosol formation from aging of aircraft exhaust

M. A. Miracolo et al.

Title Page

Abstract | Introduction

Conclusions | References

Tables | Figures

◄ | ►

◄ | ►

Back | Close

Full Screen / Esc

Printer-friendly Version

Interactive Discussion

2.2 Instrumentation

A suite of real-time instrumentation was used to monitor the evolution of the gas- and particle-phase pollutants inside the smog chamber. Measured gas-phase concentrations included CO_2 (LI-820, Li-Cor Biosciences), CO (Model 300A, API-Teledyne), NO_x (Model 200A, API-Teledyne), SO_2 (Model 100E, API-Teledyne), and O_3 (Model 400E, API-Teledyne). Quartz filter and Tenax sorbent samples were collected for offline analysis with a Gerstel Thermal Desorption System (TDS3) using a Gerstel Cooled Injection System (CIS4) connected to an Agilent 6890 gas chromatograph equipped with an Agilent 5975 mass-selective detector. In addition, samples were collected in SUMMA canisters for offline GC-MS analysis of 94 volatile organic gases. A complete list of measured VOCs is provided in the online Supplement (Presto et al., 2010).

Particle-phase measurements included a Scanning Mobility Particle Sizer (DMA Model 3081, CPC Model 3772, TSI Inc.), an in-situ OC/EC analyzer (Sunset Laboratories) to measure organic and elemental carbon (OC and EC) concentrations and a seven channel Aethalometer (Magee Scientific, Model AE-31) to measure black carbon (BC). Particle size and composition distributions of non-refractory mass were monitored using a quadrople Aerosol Mass Spectrometer (Q-AMS).

Aerosol volatility was measured using a thermodenuder (TD) system based on the design of Huffman et al. (Huffman et al., 2008). The aerosol from the chamber was alternately sampled through the TD or a bypass line maintained at ambient temperature (25 °C) every 15 min using the AMS and SMPS. The TD system was operated with two different temperature programs. Prior to photo-oxidation, the primary aerosol was characterized at 40, 60 and 80 °C. During photo-oxidation, the TD was held at 60 °C. After photo-oxidation, the aged aerosol was characterized at 40, 60 and 80 °C. The centerline residence time of the heated section was 18.6 s at ambient temperature.

3 Data analysis

Emission data are reported as fuel based emission factors. Emission factors were calculated as:

$$EF = \frac{[P]}{[\Delta CO_2]} \cdot \frac{MW_{CO_2}}{MW_C} \cdot C_f \tag{1}$$

where $[P]$ is the measured pollutant concentration inside the chamber, $[\Delta CO_2]$ is the background corrected CO_2 concentration in the chamber, MW_{CO_2}/MW_c is the ratio between the molecular weights of CO_2/C, and C_f is the carbon content of the fuel. The carbon content of the fuel was 0.86 by mass (Table A2 in the Supplement).

The AMS data were interpreted using the fragmentation table of Allan et al. (Allan et al., 2004). The contribution of gas-phase CO_2 to the m/z 44 signal was corrected using the measured CO_2 concentrations. Maximum CO_2 levels in the chamber after exhaust injection ranged from 625 to 1190 ppmv. CO_2 levels remained constant throughout a photo-oxidation experiment (<1% change over several hours).

For the 4% engine load experiments, there was significant organic particle signal at m/z 28 (CO^+) in addition to the large air beam signal (N_2+). The default fragmentation table in the unit mass resolution (UMR) analysis software assigns zero organic signal at m/z 28. However, recent analysis has shown that the organic contribution at m/z 28 can be significant for both ambient (Aiken et al., 2008; Zhang et al., 2005) and chamber data (Grieshop et al., 2009a). The organic signal at m/z 28 was treated in a similar manner as Grieshop et al. for all the 4% load experiments (Grieshop et al., 2009a). Briefly, an estimate of the organic particle signal is obtained by subtracting the gas-phase signal from the total signal at m/z 28 and then calculating an organic equivalent mass for the particle signal. The baseline for the signal at m/z 28 was determined by using a linear fit between HEPA-filtered chamber air samples taken at the beginning and end of the experiments. For the 4% load experiments, the contribution of particle signal at m/z 28 was on average 10% of the total OA. There was no particle-signal at m/z 28 in the experiments performed at higher loads (7, 30, 85%).

The SMPS data were converted to particle mass using measurements of aerosol composition measurements from the AMS and Aethalometer. The concentration of sulfate and organic mass was determined by scaling the total particle volume concentrations measured with the SMPS with measured composition ratios from the AMS between organics and sulfate. We assumed that the EC component has a density of 2.0 g cm^{-3}, the sulfate component has a density of 1.8 g cm^{-3} and the organic component has a density of 1.1 g cm^{-3}. An organic aerosol density of 1.1 g cm^{-3} was estimated with AMS and SMPS data at 4% load using the method of DeCarlo et al. and the same density was assumed for all loads (DeCarlo et al., 2004).

To estimate secondary aerosol formation, the chamber data must be corrected for loss of particles and semivolatile vapors to the smog chamber walls (Weitkamp et al., 2007). While accounting for the loss of particles to the chamber walls is relatively straightforward, losses of condensable vapors to the chamber walls can introduce significant uncertainty to the wall loss correction (Matsunaga and Ziemann, 2010). These corrections were made following the approach of Weitkamp et al. (Weitkamp et al., 2007). Briefly, the change in the suspended particle mass in the chamber (C_{sus}) is given by:

$$\frac{d}{dt}\left[C_{sus}\right] = -k_w C_{sus} + \dot{P}_{sus} \tag{2}$$

where k_w is the first order wall loss rate constant and $\dot{P}_{sus}$ is the production rate of SOA on the suspended particles. The change in mass on the walls of the chamber (C_{wall}) is given by:

$$\frac{d}{dt}\left[C_{wall}\right] = k_w C_{sus} + \dot{P}_{wall} \tag{3}$$

where $\dot{P}_{wall}$ is the loss rate of condensable vapors to the walls. A first-order wall loss rate was estimated using the measured decay of black carbon (non-reactive) as measured by the Aethalometer and/or the measured decay of primary PM mass before the lights are turned on. The AMS particle time-of-flight data indicate that the particles were

internally mixed for each experiment, therefore the same wall-loss rates were used for the organic and sulfate concentrations.

To determine the wall-loss corrected concentration in the chamber, we solve for the production rate of new mass in the chamber $\dot{P}_{wall} + \dot{P}_{sus}$. $\dot{P}_{sus}$ is calculated by numerically integrating Eq. (2) using the time-series of SMPS measurements of suspended mass concentrations. The production rate on the walls is calculated by relating particle mass on the walls to the particle mass in suspension:

$$\dot{P}_{wall} = \dot{P}_{sus} \left(\frac{\omega C_{wall}}{C_{sus}} \right) \tag{4}$$

We consider two limiting cases for calculating production rate to the walls: when the condensable products only partition to the suspended particles ($\omega = 0$) and when the material lost to the walls remains completely in equilibrium with the gas phase ($\omega = 1$) for the organic mass in the chamber. The sulfate mass in the chamber was corrected using the case of $\omega = 0$ while the organic mass in the chamber is corrected using the case of $\omega = 0$ and $\omega = 1$.

Aerosol volatility is expressed in terms of a mass fraction remaining (MFR). The MFR is defined as the ratio of the AMS organic aerosol concentration measured downstream of the TD to that measured downstream of the bypass line (C_{BP}):

$$MFR = \frac{C_{TD}}{C_{BP}} \tag{5}$$

In this work, MFRs were calculated for both total AMS OA concentrations and individual AMS mass fragments measured, such as m/z 44 and 57. For the temperatures used in this study particles losses in the TD are small (<10%) and no corrections were made for these losses (Huffman et al., 2008; An et al., 2007).

4   SOA modeling

The contribution of known SOA precursors to SOA formation was quantified using the SOA model SOAM-II (Weitkamp et al., 2007). For each precursor, SOAM-II uses yields and partitioning coefficients for a set of lumped condensable products that have been
derived from experiments conducted in laboratory smog chambers. For this work, we use an updated version of the model, which includes additional precursors and updated yield data. This version of SOAM-II uses the low- and high-NO_x volatility basis set SOA yield parameterizations of Murphy et al. (Murphy and Pandis, 2009). We have also updated these parameterizations with recently published yield data for aromatic
precursors such as xylenes and benzene (Ng et al., 2007), toluene (Hildebrandt et al., 2009), and naphthalene (Chan et al., 2009).

SOAM-II was implemented in a box model that tracks the concentration and partitioning of condensable products inside the smog chamber. The model accounts for loss of condensable product to chamber walls, using the same framework describe above.
The partitioning of condensable products is calculated using absorptive partitioning theory (Odum et al., 1996), assuming that each products forms an ideal solution with the entire organic aerosol mass.

In this work, SOAM-II accounts for oxidation of 78 SOA precursors, including alkanes, alkenes, and aromatics. A complete list of precursors is provided in Table A3 in the
Supplement. The initial concentrations in the chamber for VOC precursors are based on the SUMMA canisters data. The decay of each precursor is estimated based on OH concentrations inferred from the measured decay of SO_2 and published kinetic data.

Title Page

Abstract | Introduction

Conclusions | References

Tables | Figures

◄ | ►I

◄ | ►

Back | Close

Full Screen / Esc

Printer-friendly Version

Interactive Discussion

5 Results

5.1 Production of secondary aerosol

Figure 2 shows time-series of gas- and particle-phase concentrations from an experiment conducted with exhaust from 4% engine load. These results are representative of those obtained in other experiments. Each experiment can be divided into three different periods which are labeled on the top of Fig. 2: bag filling during which exhaust was added to the chamber, primary emission characterization during which chamber contents were characterized in the dark, and photo-oxidation during which the chamber was exposed to UV light.

Figure 2a plots the concentrations of NO, CO_2, CO, SO_2, and O_3. Concentrations of primary species (NO, CO_2, CO, SO_2) increased during bag-filling phase of the experiment when exhaust was added to the chamber. In the experiment shown in Fig. 2, the concentration of CO_2 increased from approximately 400 to 950 ppmv and then remained constant throughout the primary characterization and photochemical aging periods. When the lights were turned on, the concentration of O_3 increased, while NO decreased due to photochemistry. Photo-oxidation also reduced the concentration of SO_2; the decay of SO_2 was used to estimate OH concentrations inside the chamber for each experiment using an OH rate constant of $1.5 \times 10^{-12}\, cm^3\, molecules^{-1}\, s^{-1}$ (Seinfeld, 2006).

Time-series of particle-phase data from the AMS and SMPS are plotted in Fig. 2b, including AMS non-refractory mass, SMPS total volume and number concentrations and volume median diameter. The vertical gray bars in Fig. 2b indicate periods where the aerosol was passed through the thermodenuder. Evaporation inside the TD caused the particles to shrink and the measured non-refractory AMS mass and SMPS total volume concentrations to decrease.

Measured aerosol concentrations increased when exhaust was injected into the chamber ($t = -1.6\,h$). During the primary characterization phase of the experiment, the measured aerosol mass and number decreased, as particles were lost to the chamber

walls (Fig. 2b). Coagulation also caused the particles to grow, as the mass-weighted median diameter increased from approximately 35 to 65 nm before the lights are turned on. After the UV lights were turned on ($t = 0$ h), AMS non-refractory aerosol mass concentrations inside the chamber increased dramatically from 1 to 160 µg m^{-3} after one hour of oxidation. There was also a sharp increase in measured particle number indicating nucleation inside the chamber. The increase in AMS non-refractory mass concentrations during the first hour of photo-oxidation corresponded to an increase in aerosol concentrations of more than a factor of 100, indicating very substantial production of secondary aerosol mass.

Figure 3 plots particle size distributions measured with the SMPS for emissions at 4% load. Size distributions are plotted as fuel-based aerosol number emission factors immediately after filing the chamber, immediately before the lights were turned on, immediately after a nucleation event, and at the end of the aging portion of the experiment. Immediately after the filling period, primary PM emissions in the bag were concentrated in the nucleation mode, with a number median diameter of approximately 35 nm. During the primary characterization period, the number size distribution grew from 35 to 65 nm due to coagulation. Figure 3 shows that photo-oxidation created a bimodal size distribution with a clear nucleation mode and a larger primary mode. Photo-oxidation caused rapid and substantial growth in the median particle diameter. Both the nucleation and primary mode continued to grow and mix throughout the photo-oxidation period due to both coagulation and condensational growth.

Figure 4 plots time-series of the wall-loss corrected aerosol mass inside the chamber as fuel-based emission factors. All of the data are wall-loss corrected assuming $\omega = 0$, which provides a conservative, lower-bound estimate of the formation of secondary aerosol because it does not account for the loss of condensable vapors to the chamber. To quantify the relative importance of secondary PM production, the ratio of the secondary-to-primary PM is plotted on the right axis.

Photo-oxidation created substantial secondary aerosol mass in every experiment. At the end of the experiment, the ratio of secondary to primary PM mass was on average

35 ± 4.1, 17 ± 2.5, 60 ± 2.2, and 2.7 ± 1.1 times greater than the primary PM for the 4, 7, 30, and 85% load experiments, respectively. These uncertainty values account for both the uncertainty in the estimate of the wall-loss rate and the uncertainty of the calculation of $\omega = 0$ and $\omega = 1$ for the organic fraction of the aerosol mass.

In order to compare formation of secondary aerosol across experiments at different engine loads, one must account for differences in hydroxyl radical (OH) concentrations. OH concentrations were inferred from the decay of SO_2 using published kinetic data. The average OH concentration for each experiment is listed in Table A1 in the Supplement. OH concentrations for 4% load experiments were an order of magnitude higher ($\sim 10^7$ molecules cm^{-3}) than for the higher load (7, 30, 85%) experiments ($\sim 10^6$ molecules cm^{-3}). We attribute this difference to the much higher VOC concentrations in the chamber at 4% load. Therefore, several hours of oxidation for the 4% load experiment results in a greater integrated OH exposure ([OH] × time) than for the higher load experiments.

The top axis on Fig. 4 indicates time for OH exposure equal to one hour of 3×10^6 molecules cm^{-3}, which is typical of summertime OH concentrations. It is important to note the short time scales ($\sim$minutes) of exposure to typical oxidant conditions required for emissions of secondary aerosol to exceed primary aerosol for all engine loads. Therefore, secondary PM production must be accounted for when assessing influence of aircraft emissions on ground-level PM concentrations near airports. The impact of aircraft emissions is far greater than would be suggested by primary PM alone.

On a fuel basis, secondary aerosol production was highest at 4% load and lowest at 30% load, increasing again at 85% load. These trends were driven by differences in SOA production. The composition of secondary aerosol formed varied for each engine load. The data shown in Fig. 4 is the average of two different estimates of secondary sulfate: secondary sulfate as measured by the AMS and the decay of SO_2 as measured by the SO_2 monitor. We averaged these two estimates because of low signal-to-noise in the AMS in certain low concentration experiments. Figure 5 compares these two

estimates. The solid line is the calculated sulfate formation based on measured SO_2 decay. Estimates of secondary sulfate based on the AMS data are also shown for each experiment, except experiments #1 and #2 when SO_2 decay was not measured. An estimate for the uncertainty associated with the last measured point for each experiment

5　is also shown. For the 4% load experiments, the sulfate estimate based on AMS data agree well with the estimate from the SO_2 monitor at the end of the photo-oxidation period (SO_2 decay around 200 mg/kg-fuel). For the higher load experiments (7, 30 and 85%), the AMS estimate of sulfate was slightly higher than the SO_2 monitor estimate. The significant production of secondary sulfate at each load was due to the significant

10　sulfur content of the fuel (608 ppmw).

　　For emissions at 4% load, SOA formation dominated the secondary aerosol production (Fig. 4a). At higher loads, sulfate contributed the majority of the secondary PM mass. Since sulfate formation is a function of fuel sulfur content and OH exposure (and not engine load), the trends in total PM production are driven by differences in

15　SOA production.

　　Figure 6a compares total SOA production as a function of engine load as measured at the end of each experiment. Figure 6b plots emissions of single-ring aromatic compounds as determined by the analysis of the SUMMA canisters, including toluene, benzene, and xylenes. These emissions of single-ring aromatics were highest at 4%

20　load, more than a factor of two greater than the emissions at higher loads. This is consistent with previous studies (Anderson et al., 2006; Herndon et al., 2006; Agrawal et al., 2008) that have shown significant amounts of light hydrocarbon emissions at low load, and lower emissions at higher loads.

　　The variation in SOA production with load qualitatively mirrors the emissions of

25　single-ring aromatics; a peak at 4% load and a minimum at 30% engine load. However, Fig. 6 indicates that emissions of single-ring aromatics alone cannot describe the measured amount of SOA formation. For example, at 4% load not only would the single-ring aromatics have to be completely oxidized during the aging portion of the experiment, but the SOA yields from these compounds would need to be greater

than 100% to explain the amount of SOA formed. Therefore, other precursors must contribute significantly to SOA formation.

Emissions of low-volatility organic vapors (species that elute from the GC column after a C_{12} n-alkane) were quantified by GC-MS analysis of samples collected on Tenax sorbent tubes. We refer to this material as intermediate volatility organic compounds (IVOCs). The vast majority (>90%) of the IVOC appear as an "unresolved complex mixture" or UCM that cannot be quantified on a molecular level. Therefore, we developed calibration factors for the IVOC UCM using fuel and oil samples. Details of the analysis are described elsewhere (Presto et al., 2010).

Figure 6b plots the total emissions of IVOCs determined from the analysis of the Tenax sorbent samples as a function of engine load. This includes speciated compounds as well as IVOC UCM. Emissions of IVOCs were highest at 4% load and fell sharply with load, with a minimum at 30%. The trend in IVOC emissions mirrors the changes in SOA production with load. Therefore, these compounds are likely important SOA precursors; however more research into the SOA potential of this class of compounds is needed.

5.2 Organic aerosol composition and volatility

Figure 7 plots organic aerosol mass spectra measured using the AMS. A comparison of primary and aged OA mass spectra is shown in Fig. 7a based on the average of the three 4% load experiments. The primary organic aerosol mass spectrum was dominated by the series of peaks at C_nH_{2n-1} and C_nH_{2n+1} mass fragments, which are typical of fresh hydrocarbon-like aerosol (Zhang et al., 2005). Photo-oxidation increases the AMS signal at oxygenated fragments (m/z 29, 43, 44, etc.) and decreases the signal in the fragments associated with the primary emissions (m/z 41, 55, 57, etc.). These general trends are similar to that observed during photo-oxidation of emissions from other combustion sources (Sage et al., 2008; Grieshop et al., 2009b).

Figure 7b shows the average time evolution of AMS fragments m/z 44 and 57 for the 4% load experiments. The AMS signal at m/z 44 (CO_2^+) is a widely used marker for

Full Screen / Esc

Printer-friendly Version

Interactive Discussion

the extent of oxygenation in organic aerosol (Zhang et al., 2005), while the signal at m/z 57 is used as a tracer for primary organic aerosol (POA) (Sage et al., 2008). The data show a dramatic change in organic aerosol composition during the first 20 min of oxidation due to SOA production, with the contribution of m/z 57 decreasing from approximately 5% to 1.4% and the contribution of m/z 44 increasing from 6% in the POA to approximately 8.5% in the aged aerosol. Note that after approximately 20 min of oxidation, the aerosol inside the chamber is dominated by SOA at 4% load (Fig. 4a), and the AMS mass spectrum of OA remains relatively constant for several hours of oxidation, even though SOA continues to be produced in the chamber. The time-resolved profile of m/z 44 is different than that of other combustion sources, such as diesel exhaust (Sage et al., 2008) and woodsmoke (Grieshop et al., 2009a), which show a more gradual increase in the contribution of m/z 44. This difference is most likely due to the SOA rapidly overwhelming the POA in the aircraft exhaust whereas POA contributes a larger fraction of the OA in the other combustion systems.

Changes in aerosol volatility are shown in Fig. 8a, which plots OA mass fraction remaining (MFR) as a function of temperature (thermograms) for POA, aged OA, and the AMS fragments m/z 44 and 57 for aerosol sampled at 4% engine load. The data shown in this figure are from experiment #4, but similar trends were observed for all experiments performed at 4% engine load.

The TD data indicate that both primary and aged aircraft OA are semivolatile and that photo-oxidation reduces volatility of the OA. Therefore, the SOA has a lower volatility than the POA. For example at 80 °C, about 40% of the aged OA evaporated, compared to about 70% of the primary OA. However, at lower temperatures (40 and 60 °C) the same amount of OA evaporates from the fresh POA and SOA. Therefore the differences in volatility appear to be due to a "tail" of lower volatility material. Similar to other types of OA, the compounds that contribute to the AMS signal at m/z 44 are less volatile than the total OA, while the material contributing to the m/z 57 signal is more volatile. This behavior is similar to data from laboratory experiments of woodsmoke aging (Grieshop et al., 2009a) and ambient measurements.

Changes in aerosol volatility as a function of time are shown in Fig. 8b. The figure plots the evolution of organic aerosol MFR at 60 °C throughout the photo-oxidation period. The dip in these data immediately after photo-oxidation begins suggests that the initial SOA formed in the chamber is much less volatile than the POA or the SOA

5 formed in the later stages of the experiment. It is interesting to note this trend is the opposite of that shown in m/z 44 time-series (Fig. 7b). This indicates that the low-volatility SOA formed immediately after the lights are turned on is comprised of relatively reduced compounds. As the SOA becomes more oxidized, the MFR at 60 °C increases to around the same value as the primary aerosol.

10 **5.3 Modeling secondary aerosol formation**

To illustrate the fraction of SOA formation that can be explained by traditional SOA precursors, Fig. 9 plots the predictions for SOA formation at (a) 4% and (b) 85% engine load using the model SOAM-II and the measured aromatic, olefin, and alkane concentrations. The dashed area shown represents the range of OA estimates due

15 to uncertainty in wall-loss corrections. SOA formation depends on VOC-to-NO_x ratios, which varied as a function of load. At 4% load, the initial VOC/NO_x was greater than 7 ppbC/ppb-NO_x, so low-NO_x yields were used in SOAM-II. At 85% load, the initial VOC/NO_x was < 0.01 ppbC/ppb-NO_x, so high-NO_x yields were used in SOAM-II.

In both cases, the model under-predicts the extent of SOA formation measured in

20 the chamber using the traditional precursors listed in Table A3. For example, after 3 h of oxidation, the model can only explain ~40% of the measured SOA for the 4% load experiment and ~60% of the measured SOA for the 85% load experiment. The contribution of different classes of SOA precursors to the total predicted SOA differs for the 4 and 85% load cases. The predicted SOA for the 4% load experiment (Fig. 9a) is domi-

25 nated by SOA formed from aromatic precursors, with small but significant contributions from olefins and alkanes. At 85% load (Fig. 9b), the predicted SOA is dominated by SOA formed from aromatic precursors with less contribution from olefins and alkanes. However, the model may be over-predicting the contribution of the olefins to the total

SOA formation because the lumping scheme used by SOAM-II includes some very low molecular weight olefins, such as 1-butene and 1,3-butadiene. These species are unlikely to form SOA with yields and partitioning coefficients assigned by the model. Therefore, the results shown here represent an upper bound on the modeled SOA estimates based on traditional precursors.

Traditional precursors do not explain the extent of SOA measured for both the 4% and 85% load cases. However, the model does not account for emissions of IVOCs and other less-volatile organic species. As shown in Fig. 6b, the emissions of IVOCs are very substantial. The higher amount of unexplained SOA in the 4% load case is consistent with the order of magnitude higher IVOC emissions measured in the 4% load case compared to the 85% load case (Fig. 6).

6 Discussion and conclusions

Photo-oxidation of aircraft emissions produces significant amounts of secondary aerosol, which, under typical summertime conditions, exceed the primary emissions within minutes of the exhaust leaving the engine. Therefore the production of secondary aerosol must be considered when evaluating the impact of aircraft emissions on local and regional air quality. These results also contribute to our growing understanding of the dynamic nature of PM emissions from combustion systems (Grieshop et al., 2009a; Chirico et al., 2010).

The amount and composition of the secondary aerosol formed varies for each engine load. Secondary aerosol production is highest at 4% load and minimum at 30% load. At 4% load, the secondary aerosol is dominated by SOA while at higher loads the aerosol is dominated by secondary sulfate. Secondary sulfate production was consistently high across all engine loads due to the relatively high sulfur content of the fuel. Reducing fuel sulfur levels will reduce the formation of secondary aerosol. However, reducing the fuel sulfur levels, even to trace levels, would not alter the conclusion that secondary aerosol production dominates primary emissions, as the production of SOA exceeds the primary PM mass emissions at every engine load.

Title Page

Abstract | Introduction

Conclusions | References

Tables | Figures

◀ | ▶

◀ | ▶

Back | Close

Full Screen / Esc

Printer-friendly Version

Interactive Discussion

Oxidation of traditional SOA precursors cannot explain the extent of SOA formation observed. This provides further evidence of the importance of non-traditional precursors. Aircraft emit substantial amounts of low-volatility compounds, which creates a significant pool of SOA precursors that are not accounted for in traditional SOA models and traditional emissions data (Robinson et al., 2010). Very high SOA formation was observed at the lowest engine loads, which correspond to ground-level operation conditions. The results suggest that SOA formation from aircraft likely have a substantial impact on ground-level PM concentrations near airports. However, the failure of SOAM-II to explain the measured SOA production indicates that existing 3-D chemical transport models likely under-predict SOA from the aging of aircraft emissions.

Supplementary material related to this article is available online at: http://www.atmos-chem-phys-discuss.net/10/27893/2010/ acpd-10-27893-2010-supplement.pdf.

Title Page

Abstract | Introduction

Conclusions | References

Tables | Figures

◄ | ►►

◄ | ►

Back | Close

Full Screen / Esc

Printer-friendly Version

Interactive Discussion

References

Agrawal, H., Sawant, A. A., Jansen, K., Wayne Miller, J., and Cocker Iii, D. R.: Characterization of chemical and particulate emissions from aircraft engines, Atmos. Environ., 42, 4380–4392, 2008.

Aiken, A. C., Decarlo, P. F., Kroll, J. H., Worsnop, D. R., Huffman, J. A., Docherty, K. S., Ulbrich, I. M., Mohr, C., Kimmel, J. R., Sueper, D., Sun, Y., Zhang, Q., Trimborn, A., Northway, M., Ziemann, P. J., Canagaratna, M. R., Onasch, T. B., Alfarra, M. R., Prevot, A. S., Dommen, J., Duplissy, J., Metzger, A., Baltensperger, U., and Jimenez, J. L.: O/c and om/oc ratios of primary, secondary, and ambient organic aerosols with high-resolution time-of-flight aerosol mass spectrometry, Environ. Sci. Technol., 42, 4478–4485, 2008.

Allan, J. D., Delia, A. E., Coe, H., Bower, K. N., Alfarra, M. R., Jimenez, J. L., Middlebrook, A. M., Drewnick, F., Onasch, T. B., Canagaratna, M. R., Jayne, J. T., and Worsnopf, D. R.: A generalised method for the extraction of chemically resolved mass spectra from aerodyne aerosol mass spectrometer data, J. Aerosol Sci., 35, 909–922, doi:10.1016/J.Jaerosci.2004.02.007, 2004.

An, W. J., Pathak, R. K., Lee, B.-H., and Pandis, S. N.: Aerosol volatility measurement using an improved thermodenuder: Application to secondary organic aerosol, J. Aerosol Sci., 38, 305–314, 2007.

Anderson, B. E., Chen, G., and Blake, D. R.: Hydrocarbon emissions from a modern commercial airliner, Atmos. Environ., 40, 3601–3612, 2006.

Anderson, B. E., Branham, H. S., Hudgins, C. H., Plant, J. V., Ballenthin, J. O., Miller, T. M., Viggiano, A. A., Blake, D. R., Boudries, H., Canagaratna, M., et al.: Experiment to characterize aircraft volatile aerosol and trace-species emissions (excavate), NASA TM-2005-213783, 2005.

Carslaw, D. C., Beevers, S. D., Ropkins, K., and Bell, M. C.: Detecting and quantifying aircraft and other on-airport contributions to ambient nitrogen oxides in the vicinity of a large international airport, Atmos. Environ., 40, 5424–5434, 2006.

Chan, A. W. H., Kautzman, K. E., Chhabra, P. S., Surratt, J. D., Chan, M. N., Crounse, J. D., Kürten, A., Wennberg, P. O., Flagan, R. C., and Seinfeld, J. H.: Secondary organic aerosol formation from photooxidation of naphthalene and alkylnaphthalenes: implications for oxidation of intermediate volatility organic compounds (IVOCs), Atmos. Chem. Phys., 9, 3049–3060, doi:10.5194/acp-9-3049-2009, 2009.

Chirico, R., DeCarlo, P. F., Heringa, M. F., Tritscher, T., Richter, R., Prevot, A. S. H., Dommen, J., Weingartner, E., Wehrle, G., Gysel, M., Laborde, M., and Baltensperger, U.: Impact of aftertreatment devices on primary emissions and secondary organic aerosol formation potential from in-use diesel vehicles: results from smog chamber experiments, Atmos. Chem. Phys. Discuss., 10, 16055–16109, doi:10.5194/acpd-10-16055-2010, 2010.

DeCarlo, P., Slowik, J., Worsnop, D., Davidovits, P., and Jimenez, J.: Particle morphology and density characterization by combined mobility and aerodynamic diameter measurements. Part 1: Theory, Aerosol Sci. Tech., 38, 1185–1205, 2004.

Dodson, R. E., Andres Houseman, E., Morin, B., and Levy, J. I.: An analysis of continuous black carbon concentrations in proximity to an airport and major roadways, Atmos. Environ., 43, 3764–3773, 2009.

Grieshop, A. P., Donahue, N. M., and Robinson, A. L.: Laboratory investigation of photochemical oxidation of organic aerosol from wood fires 2: analysis of aerosol mass spectrometer data, Atmos. Chem. Phys., 9, 2227–2240, doi:10.5194/acp-9-2227-2009, 2009a.

Grieshop, A. P., Logue, J. M., Donahue, N. M., and Robinson, A. L.: Laboratory investigation of photochemical oxidation of organic aerosol from wood fires 1: measurement and simulation of organic aerosol evolution, Atmos. Chem. Phys., 9, 1263–1277, doi:10.5194/acp-9-1263-2009, 2009c.

Herndon, S. C., Rogers, T., Dunlea, E. J., Jayne, J. T., Miake-Lye, R., and Knighton, B.: Hydrocarbon emissions from in-use commercial aircraft during airport operations, Envir. Sci. Tech., 40, 4406–4413, doi:10.1021/es051209l, 2006.

Herndon, S. C., Wood, E. C., Northway, M. J., Miake-Lye, R., Thornhill, L., Beyersdorf, A., Anderson, B. E., Dowlin, R., Dodds, W., and Knighton, W. B.: Aircraft hydrocarbon emissions at oakland international airport, Envir. Sci. Tech., 43, 1730–1736, doi:10.1021/es801307m, 2009.

Hildebrandt, L., Donahue, N. M., and Pandis, S. N.: High formation of secondary organic aerosol from the photo-oxidation of toluene, ACP, 9, 2973–2986, 2009.

Hu, S., Fruin, S., Kozawa, K., Mara, S., Winer, A. M., and Paulson, S. E.: Aircraft emission impacts in a neighborhood adjacent to a general aviation airport in southern california, Environmental Science & Technology, 43, 8039–8045, doi:10.1021/es900975f, 2009.

Huffman, J. A., Ziemann, P. J., Jayne, J. T., Worsnop, D. R., and Jimenez, J. L.: Development and characterization of a fast-stepping/scanning thermodenuder for chemically-resolved aerosol volatility measurements, Aerosol Sci. Tech., 42, 395–407, 2008.

Secondary aerosol formation from aging of aircraft exhaust

M. A. Miracolo et al.

Title Page

Abstract	Introduction
Conclusions	References
Tables	Figures

◄◄ ► ►▌

◄ ►

Back Close

Full Screen / Esc

Printer-friendly Version

Interactive Discussion

Kinsey, J. S., Dong, Y., Williams, D. C., and Logan, R.: Physical characterization of the fine particle emissions from commercial aircraft engines during the aircraft particle emissions experiment (apex) 1–3, Atmos. Environ., 44, 2147–2156, 2010.

Matsunaga, A. and Ziemann, P.: Gas-wall partitioning of organic compounds in a teflon film chamber and potential effects on reaction product and aerosol yield measurements, Aerosol Sci. Tech., 44, 881–892, 2010.

Murphy, B. N. and Pandis, S. N.: Simulating the formation of semivolatile primary and secondary organic aerosol in a regional chemical transport model, Envir. Sci. Tech., 43, 4722–4728, doi:10.1021/es803168a, 2009.

Ng, N. L., Kroll, J. H., Chan, A. W. H., Chhabra, P. S., Flagan, R. C., and Seinfeld, J. H.: Secondary organic aerosol formation from m-xylene, toluene, and benzene, Atmos. Chem. Phys., 7, 3909–3922, doi:10.5194/acp-7-3909-2007, 2007.

Odum, J. R., Hoffmann, T., Bowman, F., Collins, D., Flagan, R. C., and Seinfeld, J. H.: Gas/particle partitioning and secondary organic aerosol yields, Envir. Sci. Tech., 30, 2580–2585, doi:10.1021/es950943+, 1996.

Onasch, T. B., Jayne, J. T., Herndon, S., Worsnop, D. R., Miake-Lye, R. C., Mortimer, I. P., and Anderson, B. E.: Chemical properties of aircraft engine particulate exhaust emissions, J. Propul. Power, 25, 1121–1137, doi:10.2514/1.36371, 2009.

Petzold, A. and Schvöder, F. P.: Jet engine exhaust aerosol characterization, Aerosol Sci. Tech., 28, 62–76, 1998.

Presto, A. A., Nguyen, N., Ranjan, M., Reeder, A., Lipsky, E. M., Hennigan, C. J., Miracolo, M. A., and Robinson, A. L.: Particulate and organic vapor emissions from an in-use aircraft engine, Atmos. Environ., submitted, 2010.

Robinson, A. L., Grieshop, A. P., Donahue, N. M., and Hunt, H. W.: Updating our conceptual model for fine particle mass emissions from combustion systems, J. Air Waste Manage. Assoc., accepted, 2010.

Sage, A. M., Weitkamp, E. A., Robinson, A. L., and Donahue, N. M.: Evolving mass spectra of the oxidized component of organic aerosol: results from aerosol mass spectrometer analyses of aged diesel emissions, Atmos. Chem. Phys., 8, 1139–1152, doi:10.5194/acp-8-1139-2008, 2008.

Seinfeld, J. H., Pandis, S. N., and Sypros, N.: Atmospheric chemistry and physics, John Wiley & Sons, Inc., 2006.

Slemr, F., Giehl, H., Slemr, J., Busen, R., Schulte, P., and Haschberger, P.: In-flight mea-

Secondary aerosol formation from aging of aircraft exhaust

M. A. Miracolo et al.

surement of aircraft non-methane hydrocarbon emission indices, Geophys. Res. Lett., 25, 321–324, doi:10.1029/97gl03784, 1998.

Spicer, C. W., Holdren, M. W., Riggin, R. M., and Lyon, T. F.: Chemical composition and photochemical reactivity of exhaust from aircraft turbine engines, Ann. Geophys., 12, 944–955, doi:10.1007/s00585-994-0944-0, 1999.

Unal, A., Hu, Y., Chang, M. E., Talat Odman, M., and Russell, A. G.: Airport related emissions and impacts on air quality: Application to the atlanta international airport, Atmos. Environ., 39, 5787–5798, 2005.

Wayson, R. L., Fleming, G. G., and Iovinelli, R.: Methodology to estimate particulate matter emissions from certified commercial aircraft engines, J. Air Waste Manage. Assoc., 59, 91–100, doi:10.3155/1047-3289.59.1.91, 2009.

Weitkamp, E. A., Sage, A. M., Pierce, J. R., Donahue, N. M., and Robinson, A. L.: Organic aerosol formation from photochemical oxidation of diesel exhaust in a smog chamber, Environ. Sci. Tech., 41, 6969–6975, 2007.

Wey, C. C., Anderson, B. E., Hudgins, C., Wey, C., Li-Jones, X., Winstead, E., Thornhill, L. K., Lobo, P., Hagen, D., Whitefield, P., Yelvington, P., E., Herndon, S. C., Onasch, T. B., Miake-Lye, R. C., Wormhoudt, J., Knighton, W. B., Howard, R., Bryant, D., Corporan, E., Moses, C., Holve, D., and Dodds, W.: Aircraft particle emissions experiment (apex), 2006.

Wood, E. C., Herndon, S. C., Timko, M. T., Yelvington, P. E., and Miake-Lye, R. C.: Speciation and chemical evolution of nitrogen oxides in aircraft exhaust near airports, Envir. Sci. Tech., 42, 1884–1891, doi:10.1021/es072050a, 2008.

Yu, K. N., Cheung, Y. P., Cheung, T., and Henry, R. C.: Identifying the impact of large urban airports on local air quality by nonparametric regression, Atmos. Environ., 38, 4501–4507, 2004.

Zhang, Q., Alfarra, M. R., Worsnop, D. R., Allan, J. D., Coe, H., Canagaratna, M. R., and Jimenez, J. L.: Deconvolution and quantification of hydrocarbon-like and oxygenated organic aerosols based on aerosol mass spectrometry, Environ. Sci. Tech., 39, 4938–4952, 2005.

Title Page

Abstract | Introduction

Conclusions | References

Tables | Figures

|◄ | ►|

◄ | ►

Back | Close

Full Screen / Esc

Printer-friendly Version

Interactive Discussion

CMU Mobile Laboratory

Portable Smog chamber

Q-AMS

SMPS

In Situ OC/EC

Gas monitors NOx, CO, CO2, SO2

UV lights

Inlet at 1 meter

Heated transfer line

**Ejector dilutors**

Sampling line
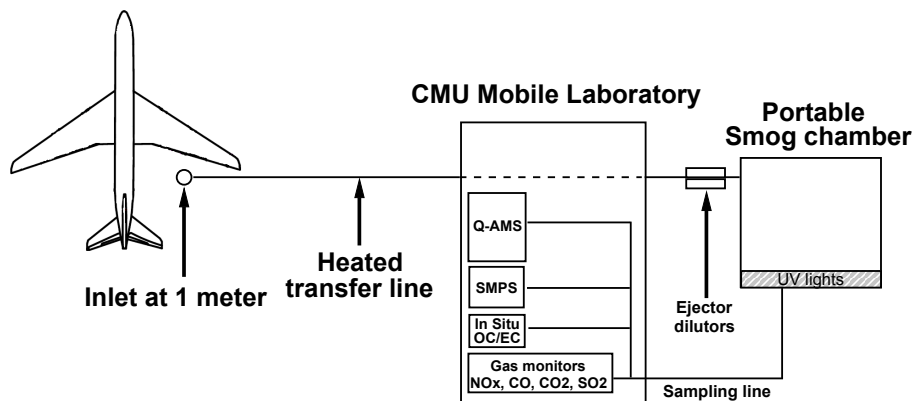
Fig. 1. Schematic diagram of experimental setup for the field campaign. Emissions were sampled from a KC-135 Stratotanker port inboard engine through an inlet installed one-meter downstream of the engine exit plane. Emissions were transferred into a portable smog chamber and monitored throughout the experiment with instruments onboard the CMU Mobile Laboratory.

Full Screen / Esc

Printer-friendly Version

Interactive Discussion
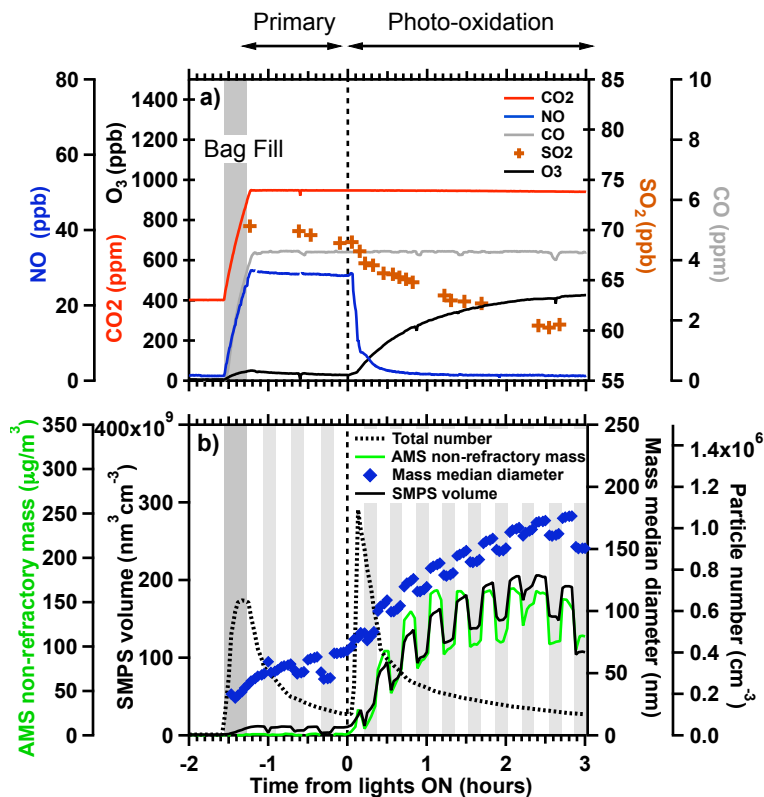
Fig. 2. Time series of **(a)** gas and **(b)** particle-phase concentrations measured for a typical photo-oxidation experiment conducted at 4% engine load. Vertical gray bars indicate period when bag is filled with exhaust or where aerosol was passed through the thermodenuder.
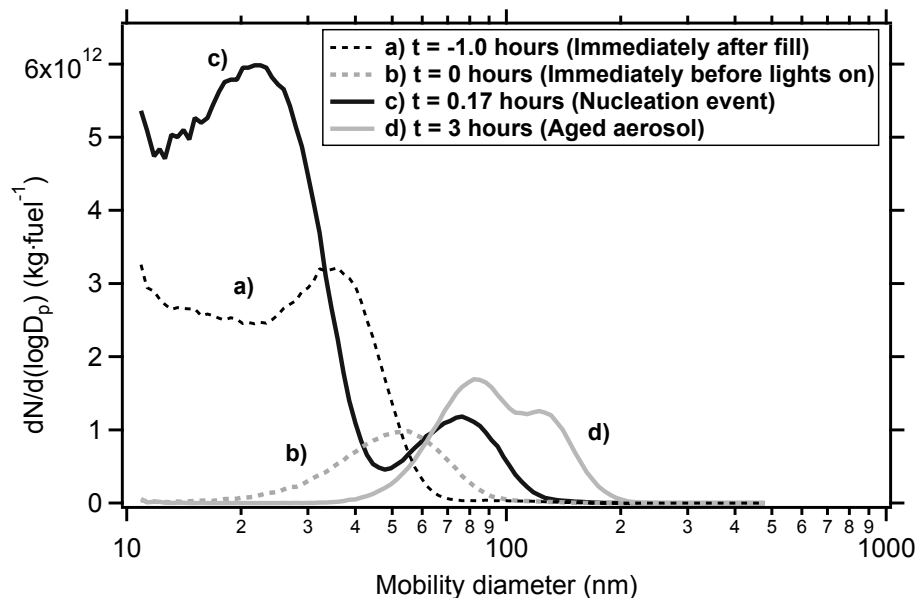
Fig. 3. Size distributions for emissions **(a)** immediately after fill, **(b)** immediately before lights on, **(c)** nucleation event, and **(d)** aged aerosol at 4% engine load. Aged aerosol corresponds to the average size distribution after 3 h of oxidation. The decrease in particle number is due to a combination of coagulation and particle losses to the chamber walls.
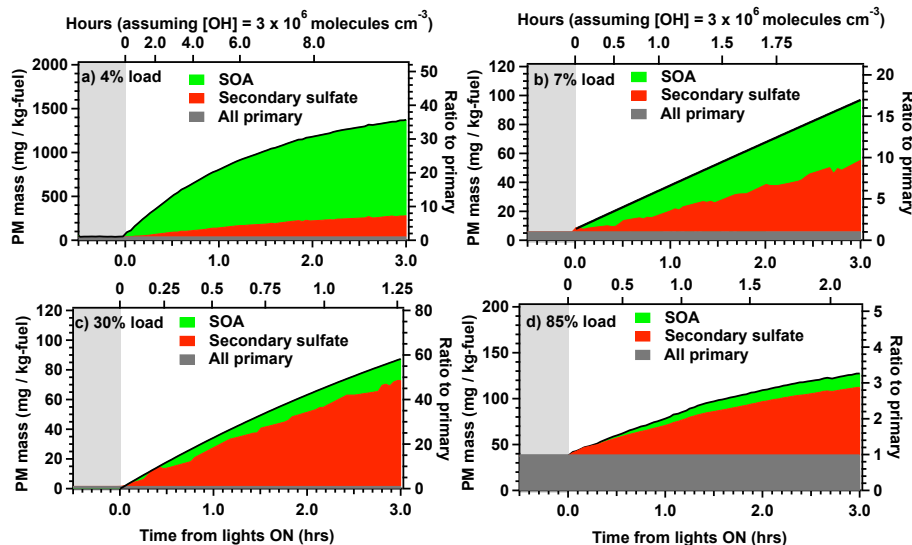
Fig. 4. Measured changes in the PM mass (secondary organics and secondary sulfate) caused by photo-oxidation for four engine loads: **(a)** 4% load, **(b)** 7% load, **(c)** 30% load, **(d)** 85% load. The data have been wall-loss corrected. Top axis indicates time for OH exposure assuming a constant [OH] concentration of 3×10^6 molecules cm^{-3}. The ratio of secondary-to-primary PM is plotted on the right axis. Note different scales on each panel.
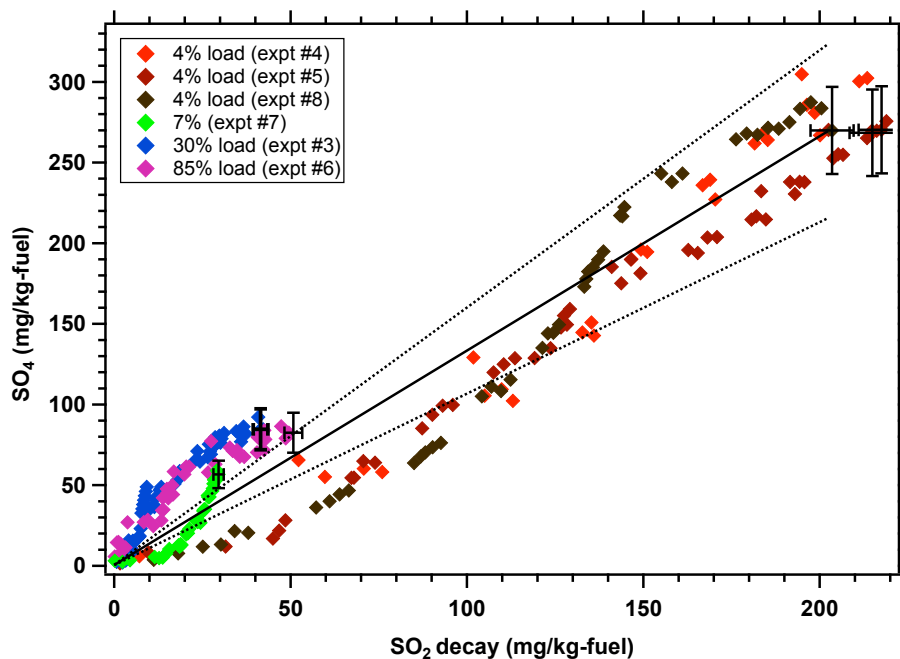
Fig. 5. Comparison of sulfate production inferred from the measured SO_2 decay (x-axis) and measurement with the AMS. If the two estimates agreed, the data fall along the solid line. The dashed lines indicate ±20%.
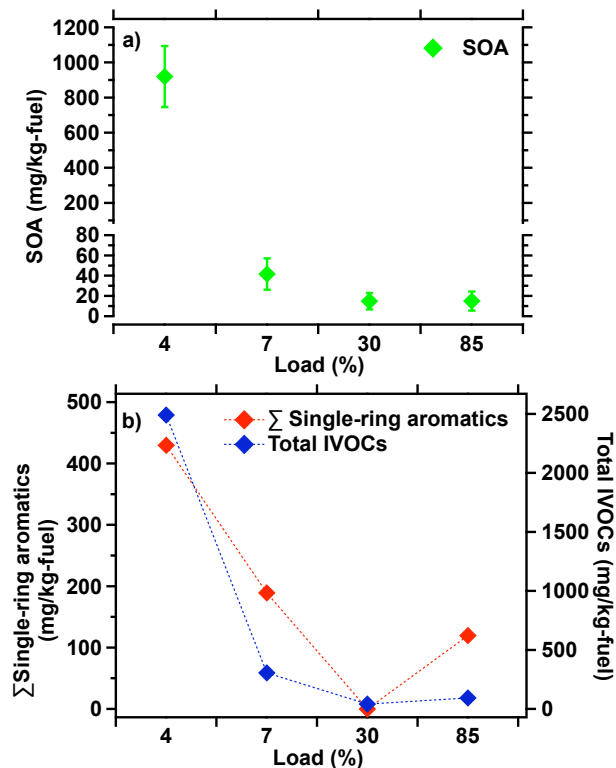
Fig. 6. (a) SOA production as a function of engine load as measured at the end of the aging phase of the experiment. **(b)** Sum of single-ring aromatic compounds and sum of IVOC emissions as a function of load. Single-ring aromatics include benzene, toluene, xylenes, ethyl benzene, styrene, ethyl toluene, and trimethyl benzenes. Sum of IVOCs includes speciated compounds and IVOC unresolved complex mixture (UCM).

Title Page

Abstract | Introduction

Conclusions | References

Tables | Figures

|◄ | ►|

◄ | ►

Back | Close

Full Screen / Esc

Printer-friendly Version

Interactive Discussion
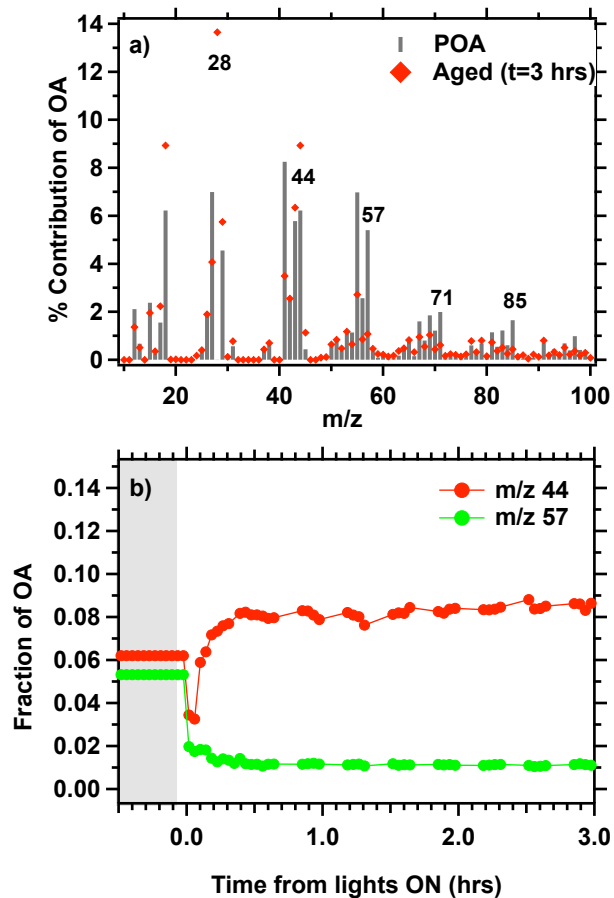
Fig. 7. (a) AMS mass spectra of primary and aged OA at 4% engine load. **(b)** Time evolution of AMS mass fragments 44 and 57 for 4% load. Data are averages of all experiments conducted at 4% load. Only undenueded (no TD) data are shown.
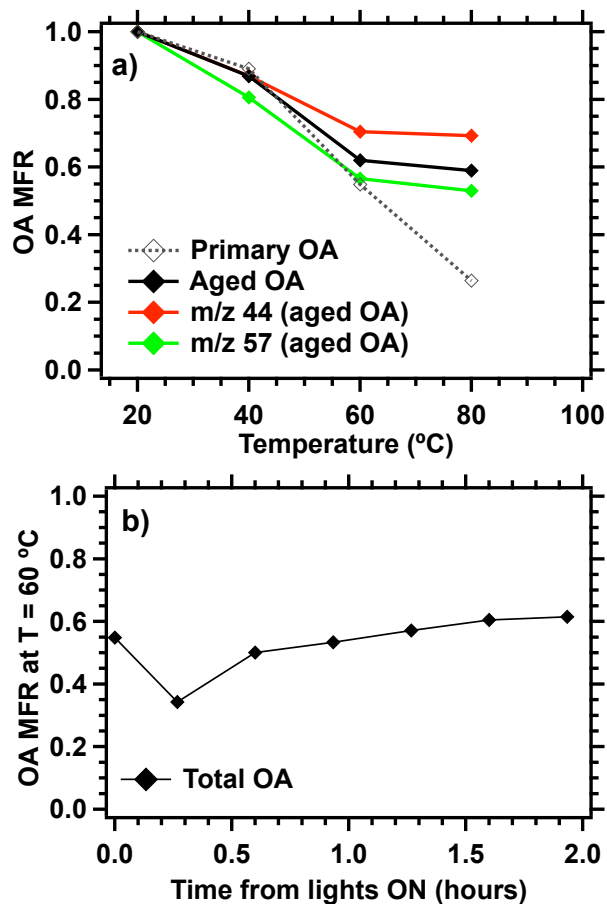
Fig. 8. (a) Average TD thermograms for primary OA, aged OA, and AMS fragments *m/z* 44 and 57 for the aged aerosol for 4% engine load. **(b)** Evolution of total OA volatility for thermodenuder temperature hold at $T = 60\,^\circ$C during oxidation. Lines are included to help guide the eye.
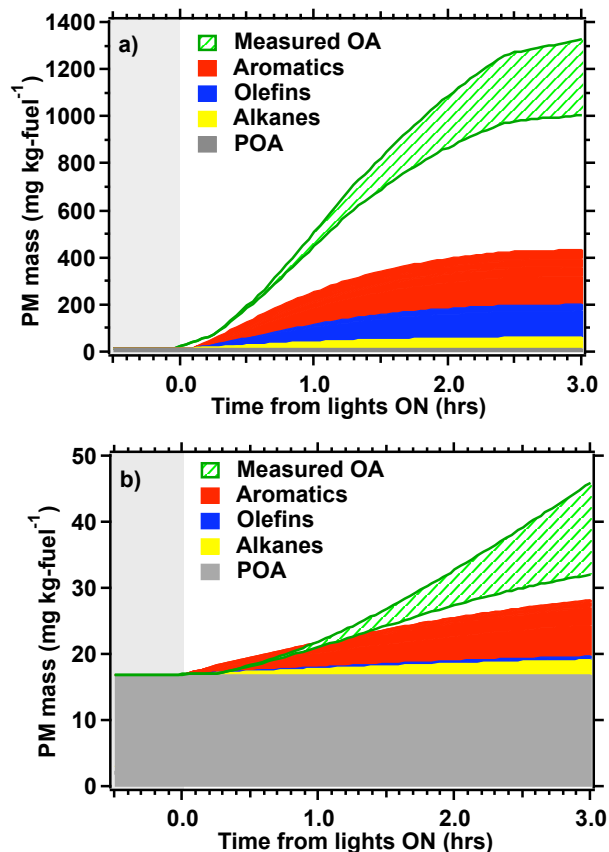
Fig. 9. Comparisons of predictions of SOA model to measurement data at **(a)** 4% engine load (low-NO$_x$) and **(b)** 85% load (high-NO$_x$). Dashed area represents range of measured OA estimates and accounts for uncertainty in wall-loss corrections. Different colored areas indicate the predicted concentrations of aromatic, olefin, and alkane precursors to the predicted SOA.

Title Page

Abstract | Introduction

Conclusions | References

Tables | Figures

|◄ | ►|

◄ | ►

Back | Close

Full Screen / Esc

Printer-friendly Version

Interactive Discussion